

Anna Vesala

PHASE-MATCHED METAMATERIALS FOR SECOND-HARMONIC GENERATION

Faculty of Engineering and Natural Sciences (ENS)
Bachelor of Science Thesis
April 2020

ABSTRACT

Anna Vesala: Phase-matched Metamaterials for Second-harmonic Generation
Bachelor of Science Thesis
Tampere University
Bachelors Degree Programme in Science and Engineering
Major: Physics
Examiners: Dr. Mikko Huttunen and M.Sc. Timo Stolt
April 2020

Metamaterials exhibit unconventional electromagnetic properties that cannot be found in nature, such as negative index of refraction or strong optical activity. Moreover, they show promise for enabling nanoscale nonlinear optics. Current nonlinear optical interactions of practical use rely on phase matching combined with long propagation lengths, which are not compatible with the size requirements of miniaturized systems. In order to be able to improve the realizable conversion efficiencies of nonlinear processes and discover novel functionalities at the nanoscale, new kinds of nonlinear metamaterials need to be investigated.

By utilizing local-field enhancements and the phase engineering of localized surface plasmon resonances, it is possible to construct metamaterials which generate nonlinear frequencies into the direction where the fundamental light came from. In this Thesis, we demonstrate how phase matching is achieved in nanoscale nonlinear materials. Especially, we fabricate three-dimensional plasmonic metamaterial devices that were phase matched for back-propagating second harmonic-generation. Our samples consist of one to five metasurfaces stacked on top of each other and the aim was to observe how the intensity of the second-harmonic field varies with the number of metasurfaces stacked in a backward phase-matched metamaterial.

The results show that the second harmonic signal depends quadratically on the number of metasurfaces, which confirms that the sample was successfully phase-matched by controlling the dimensions of the nanoparticles and the separation between the metasurfaces. This provides insight into how the performance of nonlinear metamaterials can be increased considerably by stacking metasurfaces inside of a three-dimensional metamaterial. Furthermore, the measurements provided experimental confirmation for backward phase matching, where the fundamental and second-harmonic waves were counter-propagating. These results demonstrate a completely novel principle for improving the conversion efficiencies of nanoscale nonlinear materials.

Keywords: Nonlinear optics, metamaterials, metal nanoparticles, phase matching, second-harmonic generation.

The originality of this thesis has been checked using the Turnitin OriginalityCheck service.

PREFACE

This Thesis has been conducted in the Nonlinear Optics research group of the Laboratory of Photonics at Tampere University under the supervision of Dr. Mikko Huttunen and M.Sc. Timo Stolt. It has been written to fulfill the graduation requirements of the International Bachelor's Degree Programme in Science and Engineering. All of the research presented henceforth was done in collaboration with a large group of people: Timo Stolt, Jeonghyun Kim, Sébastien Héron, Mikko Huttunen, Robert Czaplicki, Martti Kauranen, Junsuk Rho, and Patrice Genevet. I was responsible for data collection and analysis and most of the experimental work for this Thesis was performed in May–July 2019.

In reality, I would not have been able to achieve my current level of success without a strong team behind me. First of all, I would like to thank Mikko for not only his support and advice throughout the writing of this Thesis but also for the entire time I have worked with the research group. Secondly, I would like to thank all of my colleagues in the Photonics Laboratory for creating a positive work environment for me. I would especially like to thank Timo and Antti, who have always been patient and helped guide me through the practicalities of working in a research group. Lastly, I'd also like to thank my family and all of my friends for their unwavering support throughout my entire life.

Tampere, 27th April 2020

Anna Vesala

CONTENTS

| | | |
|-------|---|----|
| 1 | Introduction | 1 |
| 2 | Theory | 3 |
| 2.1 | Optics | 3 |
| 2.2 | Nonlinear Optics | 5 |
| 2.2.1 | Second-harmonic Generation | 5 |
| 2.2.2 | Wave Equation for Nonlinear Systems | 6 |
| 2.2.3 | Coupled-amplitude Wave Equations for Sum-frequency Generation | 8 |
| 2.2.4 | Phase Matching | 9 |
| 2.2.5 | Phase Matching in Metamaterials | 11 |
| 3 | Research Methods | 13 |
| 3.1 | Nanoparticle Array Samples | 13 |
| 3.2 | Experimental Setup and Procedure | 15 |
| 4 | Results and Discussion | 18 |
| 5 | Conclusion | 20 |
| | References | 22 |

LIST OF FIGURES

- 2.1 Backward phase-matched SHG emission from a metamaterial comprising of N stacked metasurfaces. When controlling the total phase accumulation of the fundamental beam (red arrow) and the SHG emissions (green arrows) the phase matching condition can be achieved. The total phase accumulation depends on the induced phase shifts caused by the metasurfaces (δ_ω and $\delta_{2\omega}$) and the phase accumulation due to propagation (φ_ω and $\varphi_{2\omega}$). 11
- 3.1 (a) Scanning electron micrograph showing the stacked nature of the metasurfaces from the samples that were studied. (b) Side view of the metamaterial with metasurface spacing $h = 225$ nm. (c) Each metasurface consisted of identical V-shaped gold nanoparticles with arm length L and 100 nm arm width. The nanoparticles were arranged into square lattice with $p = 1000$ nm. 13
- 3.2 Schematic of nanolayer fabrication based on electron-beam lithography. The patterning process can be repeated according to the number of layers needed in the sample and it consists of the following six main steps. (1) spin coating of PMMA and E-spacer onto a clean substrate; (2) electron beam exposure; (3) E-spacer removal and resist development; (4) deposition of chromium and gold; (5) lift-off; (6) spin coating of spin-on-glass. 14
- 3.3 The experimental setup for measuring backward SHG emissions from a sample. The setup contains lenses (L1–L6), half-wave plates (HWP1–HWP2), an aperture (A), polarizers (P1–P2), a long-pass filter (LPF), short-pass filters (SPF1–SPF2), dichroic mirror (DM) and photomultiplier tube (PMT). The solid red line shows the path for the fundamental beam and the dashed blue line shows the path for the generated back-propagating SH beam. 15
- 4.1 The reflected SHG emission power was detected as a function of the fundamental wavelength for two different samples (a) L180- N and (b) L190- N . The vertical dashed line represents the pump wavelength at which strong constructive phase matching occurs for the different samples. 18

4.2 Calculated SHG intensity enhancement as a function of the number of layers at 1119 nm for L180-*N* (blue squares) and 1141nm for L190-*N* (red circles). The enhancement for both samples is normalized to the SHG intensity from each of the samples own monolayer measurement ($N = 1$). The enhancement does not depend linearly on N (gray solid line), but rather follows the expected quadratic dependence on N (gray dotted line). 19

LIST OF SYMBOLS AND ABBREVIATIONS

| | |
|--------------|-------------------------------------|
| DM | Dichroic mirror |
| HWP | Half-wave plate |
| LPF | Long-pass filter |
| LSPR | Localized surface plasmon resonance |
| OPO | Optical parametric oscillator |
| PMT | Photomultiplier tube |
| SEM | Scanning electron microscope |
| SFG | Sum-frequency generation |
| SHG | Second-harmonic generation |
| SPF | Short-pass filter |
| | |
| B | Magnetic flux density |
| <i>c.c.</i> | Complex conjugate |
| c_0 | Speed of light |
| D | Electric displacement field |
| E | Electric field |
| ϵ_0 | Dielectric constant |
| H | Magnetic field intensity |
| J | Free current density |
| k | Wave number |
| M | Magnetization |
| P | Material polarization |
| r | Position vector |
| ρ | Free charge density |
| t | Time |
| μ_0 | Magnetic permeability |
| ω | Angular frequency |

1 INTRODUCTION

Nonlinear optics is a branch of physics that focuses on the interaction of intense light with media [1]. The modification of optical properties in nonlinear systems has been extensively studied in the past decades due to its importance in modern, light-based technologies [2]. It provides numerous photonic applications ranging from optical signal processing and laser-based techniques to far-field microscopy. These applications depend on nonlinear processes such as frequency conversion, supercontinuum, and ultra-short pulse generations to just name a few [3, 4]. The focus of this Thesis is the process of second-harmonic generation (SHG), by which two incoming photons with identical frequency are combined in the material into a single output photon with double the incident frequency.

SHG was first observed at the University of Michigan in 1961 by Peter Franken *et al.* [5], soon after the construction of the first laser by American physicist Theodore Maiman [6]. Since this discovery, research has shown that high conversion efficiencies can be obtained if intense laser light propagates through rather large crystals, and the generated nonlinear response propagates in phase [7]. Unfortunately, this makes traditional nonlinear optics incompatible for photonic integration that relies on microscale devices. Therefore, novel approaches for achieving high conversion efficiencies are required.

Nonlinear plasmonics, which deals with the coupling between electromagnetic radiation and collective electronic oscillations in metals [8], reveals a promising route for the manipulation of light at the nanoscale [9, 10, 11]. A metamaterial is any artificial material engineered to have properties not found in nature and often consists of periodic arrays of metal nanoparticles on a dielectric environment [12, 13, 14]. The optical properties of metal nanoparticles are governed by the plasmon resonances, which can result in enhanced nonlinear responses [9, 15, 16].

The past nonlinear experiments have mainly focused on flat, two-dimensional metamaterials known as metasurfaces [17]. Recent success in nanofabrication techniques has led to advances in the control of unconventional emission properties of three-dimensional metamaterials [18, 19]. As it will be seen in this Thesis, for example, nonlinear effects can be enhanced by merely altering the geometry of nanoparticles and the separation between metasurfaces in a three-dimensional plasmonic metamaterial.

This Thesis contains five chapters of which the first is this introduction. The second chapter covers the theoretical background, which explains the essentials of nonlinear optics

with an emphasis on phase-matching considerations and SHG. The third chapter describes the experimental study performed on two three-dimensional metamaterial devices designed to emit backward phase-matched SHG emissions. For each device, we altered the number of stacked layers so that five different SHG spectra could be measured. The aim of the research was to determine the changes in the intensity of SHG depending on the number of stacked metasurfaces in the metamaterial device and to verify the possibility to phase match such three-dimensional nonlinear metamaterials. The fourth chapter then describes the experimental results. In the final chapter, the summarized results and their implications for future research are discussed.

2 THEORY

In this chapter, the fundamentals of nonlinear optics are introduced through classical electrodynamics. Beginning from Maxwell's equations, the nonlinear wave equation that governs SHG will be derived. The solutions to the general wave equation will illustrate the coupled electromagnetic wave formalism. This will, in the end, lead to a thorough discussion on the importance of phase matching and ways it can be taken advantage of with metamaterials.

2.1 Optics

Optics is the study of light and how it behaves in various systems. These systems can be as simple as light progressing undisturbed through a vacuum or as complex as artificial structures within which light is absorbed, transmitted, and reflected [20].

In the wake of James C. Maxwell's work in the 19th century, it became apparent that light is electromagnetic radiation which is comprised both of magnetic \mathbf{H} and electric \mathbf{E} fields. The oscillating fields travel together perpendicular to each other in a quantum of energy called a photon [21]. For most of optics, light waves are often described only with the electric field because the magnetic field is not of practical significance [20]. The electric field of a one-dimensional plane wave travelling in the positive z -direction can be written as

$$\begin{aligned} E(z, t) &= E_0 e^{i(kz - \omega t)} + E_0 e^{-i(kz - \omega t)}, \\ E(z, t) &= E_0 e^{i(kz - \omega t)} + c.c., \end{aligned} \quad (2.1)$$

where E_0 represents the amplitude of the field, k is the wave number, t is the time and ω is the angular frequency. The *c.c.* stands for the complex conjugate and ensures that the time-dependent electric field is a real-valued quantity. The light propagates in a medium at a speed of

$$v = \frac{\omega}{k} = \frac{\omega}{k_0 n} = \frac{c_0}{n}, \quad (2.2)$$

where c_0 is the speed of light and k_0 is the wave number for light travelling in a vacuum. As can be seen in the expression above, the refractive index n describes how fast light advances through a material.

In three dimensional space, the wave vector $\mathbf{k} = k_x \hat{x} + k_y \hat{y} + k_z \hat{z}$ can replace the wave number so that $k = |\mathbf{k}|$. With this in mind, the electric field can be written as a vector

quantity according to

$$\mathbf{E}(\mathbf{r}, t) = E_0 \hat{\mathbf{p}} e^{i(\mathbf{r} \cdot \mathbf{k} - \omega t)} + c.c., \quad (2.3)$$

where \mathbf{r} is the position vector. The electric field oscillates with respect to space and time in a direction described by the polarization of light. In the equation above, this is denoted with the unit vector $\hat{\mathbf{p}}$.

Interaction between light and matter gives rise to a wide variety of observable effects from which we can deduce the optical properties of the investigated material. When light enters a dielectric medium, the internal charge distribution is altered and electric dipole moments are generated. Polarization density is the dipole moment per unit volume and it describes the response of a material to an applied electric field. The response does not occur instantaneously, but it instead takes a finite amount of time for the material to polarize. As a consequence, the resultant polarization depends on electric field strength according to [1]

$$\mathbf{P}(\mathbf{r}, t) = \epsilon_0 \int_{-\infty}^{\infty} \int_{-\infty}^{\infty} \chi^{(1)}(\mathbf{r} - \mathbf{r}', t - t') \mathbf{E}(\mathbf{r}', t') d\mathbf{r}' dt', \quad (2.4)$$

where $\chi^{(1)}$ is the linear susceptibility tensor and ϵ_0 is the dielectric constant. In other words, the polarization is a convolution of the electric field with the time- and space-dependent susceptibility. Therefore, the integral can be also written as

$$\mathbf{P}(\mathbf{r}, t) = \epsilon_0 \chi^{(1)}(\mathbf{r}, t) \circledast \mathbf{E}(\mathbf{r}, t), \quad (2.5)$$

where \circledast is the convolution operator. If \mathcal{F} denotes the Fourier transform operator over time and space, by using the convolution theorem the previous equation can be rewritten as

$$\mathcal{F}[\mathbf{P}(\mathbf{r}, t)] = \epsilon_0 \mathcal{F}[\chi^{(1)}(\mathbf{r}, t)] \cdot \mathcal{F}[\mathbf{E}(\mathbf{r}, t)], \quad (2.6)$$

which simplifies to

$$\mathbf{P}(\mathbf{k}, \omega) = \epsilon_0 \chi^{(1)}(\mathbf{k}, \omega) \cdot \mathbf{E}(\mathbf{k}, \omega). \quad (2.7)$$

It should be noted that the material polarization oscillates at the same frequency as the input electric field.

When it is assumed that the medium reacts instantaneously to the electric field strength, the polarization can be defined as

$$\mathbf{P}(\mathbf{r}, t) = \epsilon_0 \chi^{(1)}(\mathbf{r}, t) \cdot \mathbf{E}(\mathbf{r}, t) \quad (2.8)$$

without the convolution operator. This assumption also implies that the medium is dispersionless and lossless, which will also be presumed to be true in this section for conceptual clarity. However, use of the above Equation (2.7) would allow the generalization of the following treatment to dispersive and lossy materials, and even to materials with so-called non-local light-matter interactions.

2.2 Nonlinear Optics

The science of nonlinear optics builds on the foundations of optics, and it provides us with a deeper understanding of light–matter interactions. Nonlinear optics focuses on addressing the nonlinear portion of a material's response to an optical field.

By extending the definition of electronic polarization to the nonlinear regime, a wide variety of optical phenomena occurring with high intensity levels of light can be understood. Under the present assumption of instantaneous response, the optical response of a material can often be expressed more effectively as a series expansion of the polarization of a material according to

$$\mathbf{P}(\mathbf{r}, t) = \epsilon_0 \sum_{n=1}^{\infty} \chi^{(n)} \cdot \mathbf{E}^n(\mathbf{r}, t). \quad (2.9)$$

Here the response of the n^{th} power of the electric field is governed by the n^{th} order susceptibility tensors $\chi^{(n)}$ [4]. In this work, we limit our discussion to second-order processes related to $\chi^{(2)}$ and second-order nonlinear polarization $\mathbf{P}^{(2)}(t) = \epsilon_0 \chi^{(2)} \cdot \mathbf{E}^2(t)$.

2.2.1 Second-harmonic Generation

Second-harmonic generation is a nonlinear process where two photons of frequency ω are annihilated, and a photon of frequency 2ω is generated simultaneously. If an incident wave is represented as

$$E(t) = Ee^{-i\omega t} + c.c., \quad (2.10)$$

it can produce a second-order polarization according to

$$P^{(2)}(t) = 2\epsilon_0 \chi^{(2)} EE^* + (\epsilon_0 \chi^{(2)} E^2 e^{-2i\omega t} + c.c.). \quad (2.11)$$

The latter term describes the generation of radiation at frequency 2ω .

Unlike linear processes, second-order nonlinear effects are prone to symmetry constraints. In a centrosymmetric medium, for every point (x, y, z) relative to the centre of symmetry, there exists an identical point at $(-x, -y, -z)$. If the sign of the incident electric field is reversed, then the polarization should also be altered due to inversion of the field. By doing so we obtain a mathematical relation

$$-P^{(2)}(t) = \epsilon_0 \chi^{(2)} [-E(t)]^2 = \epsilon_0 \chi^{(2)} [E(t)]^2 = P^{(2)}(t), \quad (2.12)$$

which is only possible if $\chi^{(2)} = 0$. This indicates that SHG is forbidden in a centrosymmetric media [21, 22]. Therefore, traditional second-order nonlinear crystals belong to crystal point groups with broken inversion symmetry. The most commonly used crystals for frequency doubling are potassium titanyl phosphate (KTiOPO₄), lithium niobate (LiNbO₃), monopotassium phosphate (KH₂PO₄), and barium borate (BaB₂O₄) [23]. In nonlinear metamaterials, this problem is overcome by comprising the metamaterial with

non-centrosymmetric building blocks, such as V-shaped nanoparticles [15, 24, 25].

2.2.2 Wave Equation for Nonlinear Systems

Maxwell's equations are a group of four equations that create the foundations for explaining classical electromagnetism. In the differential form, they are written as [4]

$$\nabla \cdot \mathbf{D} = \rho, \quad (2.13a)$$

$$\nabla \cdot \mathbf{B} = 0, \quad (2.13b)$$

$$\nabla \times \mathbf{E} = -\frac{\partial \mathbf{B}}{\partial t}, \quad (2.13c)$$

$$\nabla \times \mathbf{H} = -\frac{\partial \mathbf{D}}{\partial t} + \mathbf{J}. \quad (2.13d)$$

Here \mathbf{B} is the magnetic flux density, and \mathbf{D} is the electric displacement field. In order to understand light–matter interactions in-depth, constitutive equations that describe the material response to an external electromagnetic fields also need to be defined [22]:

$$\mathbf{H} = \frac{1}{\mu_0} \mathbf{B} - \mathbf{M}, \quad (2.14a)$$

$$\mathbf{D} = \epsilon_0 \mathbf{E} + \mathbf{P}. \quad (2.14b)$$

In the above equations μ_0 is the magnetic permeability.

For a non-magnetic dielectric material magnetization \mathbf{M} , free current density \mathbf{J} and free charge density ρ can all be neglected. When taking the curl of Equation (2.13c) and combining it with Equations (2.13d) and (2.14a) we get

$$\nabla \times \nabla \times \mathbf{E} + \mu_0 \frac{\partial^2 \mathbf{D}}{\partial t^2} = 0. \quad (2.15)$$

The electric displacement field can be eliminated using Equation (2.14b). Furthermore, by using Maxwell's equations we can also derive the speed of an electromagnetic field, which allows for us to replace μ_0 with $1/\epsilon_0 c_0^2$. This way we can obtain a common nonlinear wave equation of the form

$$\nabla \times \nabla \times \mathbf{E} + \frac{1}{c_0^2} \frac{\partial^2 \mathbf{E}}{\partial t^2} = -\frac{1}{\epsilon_0 c_0^2} \frac{\partial^2 \mathbf{P}}{\partial t^2}. \quad (2.16)$$

By using the vector calculus identity $\nabla \times \nabla \times \mathbf{E} = \nabla(\nabla \cdot \mathbf{E}) - \nabla^2 \mathbf{E}$ and the transverse infinite plane wave approximation ($\nabla \cdot \mathbf{E} = 0$) we can further simplify the relation above to get the expression

$$\nabla^2 \mathbf{E} - \frac{1}{c_0^2} \frac{\partial^2 \mathbf{E}}{\partial t^2} = \frac{1}{\epsilon_0 c_0^2} \frac{\partial^2 \mathbf{P}}{\partial t^2}. \quad (2.17)$$

The equation above is an inhomogeneous wave equation, where the polarization is the source term for the radiation of the electromagnetic field. It is often favorable to split the contributions of the source term into its linear and nonlinear counterparts. This can be

achieved by expanding the electric polarization \mathbf{P} into a power series of the form

$$\mathbf{P} = \mathbf{P}^{(1)} + \mathbf{P}^{\text{NL}}, \quad (2.18)$$

where the nonlinear effects are represented by the higher order terms of the series. The above expansion also means that the electric displacement field can be written as

$$\mathbf{D} = \epsilon_0 \mathbf{E} + \mathbf{P}^{(1)} + \mathbf{P}^{\text{NL}} = \mathbf{D}^{(1)} + \mathbf{P}^{\text{NL}}. \quad (2.19)$$

Utilizing this quantity, Equation (2.17) becomes

$$\nabla^2 \mathbf{E} - \frac{1}{\epsilon_0 c_0^2} \frac{\partial^2 \mathbf{D}^{(1)}}{\partial t^2} = \frac{1}{\epsilon_0 c_0^2} \frac{\partial^2 \mathbf{P}^{\text{NL}}}{\partial t^2}. \quad (2.20)$$

This wave equation can be further modified for the case of an isotropic medium. The relation between $\mathbf{D}^{(1)}$ and \mathbf{E} can be expressed in terms of a dielectric constant $\epsilon^{(1)}$ as

$$\mathbf{D}^{(1)} = \epsilon_0 \epsilon^{(1)} \mathbf{E}, \quad (2.21)$$

where ϵ_0 is the permittivity of free space. The dielectric constant is related to the index of refraction according to $n^2 = \epsilon^{(1)}$. For the isotropic and dispersionless material Equation (2.20) can be rewritten as

$$-\nabla^2 \mathbf{E} + \frac{n^2}{c_0^2} \frac{\partial^2 \mathbf{E}}{\partial t^2} = -\frac{1}{\epsilon_0 c_0^2} \frac{\partial^2 \mathbf{P}^{\text{NL}}}{\partial t^2}. \quad (2.22)$$

For a dispersive medium, however, the frequency components have to be separately considered, therefore the electric field, linear electric displacement field, and polarization field are displayed as summations of their numerous frequency components

$$\mathbf{E}(\mathbf{r}, t) = \sum'_n \mathbf{E}_n(\mathbf{r}, t), \quad (2.23a)$$

$$\mathbf{D}^{(1)}(\mathbf{r}, t) = \sum'_n \mathbf{D}_n^{(1)}(\mathbf{r}, t), \quad (2.23b)$$

$$\mathbf{P}_n^{\text{NL}}(\mathbf{r}, t) = \sum'_n \mathbf{P}_n^{\text{NL}}(\mathbf{r}, t). \quad (2.23c)$$

The prime in the above equations signifies that the summation takes place only over positive frequencies. Each frequency component can then be written with respect to its complex amplitude by the relations

$$\mathbf{E}_n(\mathbf{r}, t) = \mathbf{E}_n(\mathbf{r}) e^{-i\omega_n t} + c.c., \quad (2.24a)$$

$$\mathbf{D}_n^{(1)}(\mathbf{r}, t) = \mathbf{D}_n^{(1)}(\mathbf{r}) e^{-i\omega_n t} + c.c., \quad (2.24b)$$

$$\mathbf{P}_n^{\text{NL}}(\mathbf{r}, t) = \mathbf{P}_n^{\text{NL}}(\mathbf{r}) e^{-i\omega_n t} + c.c.. \quad (2.24c)$$

When ignoring dissipation, the relationship between $\mathbf{D}_n^{(1)}$ and \mathbf{E}_n can be conveyed with a

frequency-dependent refractive index by

$$\mathbf{D}_n^{(1)}(\mathbf{r}, t) = \epsilon_0 n^2(\omega_n) \mathbf{E}_n(\mathbf{r}, t). \quad (2.25)$$

If all Equations from (2.23a) to (2.25) are introduced with Equation (2.20) we get

$$\nabla^2 \mathbf{E}_n - \frac{n^2(\omega_n)}{c_0^2} \frac{\partial^2 \mathbf{E}_n}{\partial t^2} = \frac{1}{\epsilon_0 c_0^2} \frac{\partial^2 \mathbf{P}_n^{\text{NL}}}{\partial t^2}, \quad (2.26)$$

which is our final form of the wave equation that holds for any frequency component of the electric field.

2.2.3 Coupled-amplitude Wave Equations for Sum-frequency Generation

Sum-frequency generation (SFG) is a second-order nonlinear process where two incident photons at frequencies of ω_1 and ω_2 can generate a new photon at frequency $\omega_3 = \omega_1 + \omega_2$. From this description, one may notice that SHG is just a special case of SFG in which the input frequencies are the same. In the previous section, a general nonlinear wave Equation (2.26) was derived that can help describe different nonlinear interactions. This equation must be valid for every frequency component of the field including the generated sum-frequency component. If we omit the nonlinear source term and assume that the incident wave reaches the nonlinear medium at normal incidence, then the solution for Equation (2.26) is

$$E_3(z, t) = A_3 e^{i(k_3 z - \omega_3 t)} + c.c.. \quad (2.27)$$

Equation (2.27) describes a plane wave at frequency ω_3 , which is travelling in the positive z direction. Here the amplitude of A_3 is constant and k_3 and ω_3 are related by

$$k_3 = \frac{n_3 \omega_3}{c_0}. \quad (2.28)$$

The solution to Equation (2.26) will be similar to what was provided in Equation (2.27), if the source term is not too strong. The only difference is that A_3 will now be a slowly varying function of z .

We can then define the nonlinear source term that appears in Equation (2.26) as

$$P_3(z, t) = P_3 e^{-i\omega_3 t} + c.c. \quad (2.29)$$

where the nonlinear polarization can be expressed by means of the following scalar relationship

$$P_3 = 4\epsilon_0 d_{\text{eff}} E_1 E_2. \quad (2.30)$$

The d_{eff} coefficient relates to the nonlinear susceptibility tensor by $d_{\text{eff}} = \frac{1}{2} \chi^{(2)}$, and it can be calculated for each crystal class separately [22]. The two input fields ($i = 1, 2$) can be

written as

$$E_i(z, t) = E_i e^{-i\omega_i t} + c.c. \quad \text{where} \quad E_i = A_i e^{ik_i z}. \quad (2.31)$$

This allows us to replace the amplitude of the nonlinear polarization with

$$P_3 = 4\epsilon_0 d_{\text{eff}} A_1 A_2 e^{i(k_1+k_2)z}. \quad (2.32)$$

Equations (2.27), (2.29) and (2.32) can all be substituted back into Equation (2.26), and because all fields propagate along z -coordinate, ∇^2 can be simplified to obtain

$$\begin{aligned} & \left[\frac{d^2 A_3}{dz^2} + 2ik_3 \frac{dA_3}{dz} - k_3^2 A_3 + \frac{n^2(\omega_3)\omega_3^2 A_3}{c_0^2} \right] e^{i(k_3 z - \omega_3 t)} + c.c. \\ & = \frac{-4d_{\text{eff}}\omega_3^2}{c_0^2} A_1 A_2 e^{i[(k_1+k_2)z - \omega_3 t]} + c.c. . \end{aligned} \quad (2.33)$$

As a result of Equation (2.28), the third and fourth terms cancel out in the equation above. Furthermore, the equality is maintained even if the complex conjugate terms are removed and the exponential factor $e^{-i\omega_3 t}$ is removed from each side. These steps reduce the previous equation down to

$$\frac{d^2 A_3}{dz^2} + 2ik_3 \frac{dA_3}{dz} = \frac{-4d_{\text{eff}}\omega_3^2}{c_0^2} A_1 A_2 e^{i[(k_1+k_2-k_3)z]} + c.c. . \quad (2.34)$$

The highest-order derivative can be neglected in the slowly-varying amplitude approximation regime if on the left-hand side of Equation (2.34) the first term is much smaller than the second term [1]. When this is valid, we get a coupled-amplitude equation given by

$$\frac{dA_3}{dz} = \frac{2id_{\text{eff}}\omega_3^2}{k_3 c_0^2} A_1 A_2 e^{i\Delta k z} \quad (2.35)$$

where we have defined the wavevector mismatch to be

$$\Delta k = k_1 + k_2 - k_3. \quad (2.36)$$

These last two equations demonstrate how the amplitude of A_3 varies due to its coupling to the A_1 and A_2 waves.

2.2.4 Phase Matching

To make matters less complicated, we suppose that the amplitudes of the input fields A_1 and A_2 are constant over propagation in Equation (2.35). This is a valid assumption whenever the conversion efficiencies for the sum-frequency field are not substantial. For the case when

$$\Delta k = 0, \quad (2.37)$$

the amplitude of the sum-frequency wave is increased linearly with respect to z [22]. The condition described by Equation (2.37) is known as perfect phase matching and when this holds the generated waves are capable of extracting the most energy from the incident waves [1]. This is attainable only if the atomic dipoles in the medium are able to maintain a proper phase in a way that the generated field by each dipole constructively combines together along the propagating direction. The resultant power emitted by all of the atomic dipoles would then depend quadratically on the number of atoms that partake in the event [22].

In order to comprehend the importance of phase matching, we need to derive an equation that expresses the intensity of the sum-frequency wave I_3 as a function of the wavevector mismatch Δk . This can be done by first integrating Equation (2.35) from $z = 0$ to $z = L$ in order to obtain the amplitude for the sum-frequency (ω_3) field. This gives

$$A_3(L) = \frac{2id_{\text{eff}}w_3^2A_1A_2}{k_3c_0^2} \int_0^L e^{i\Delta kz} dz = \frac{2id_{\text{eff}}w_3^2A_1A_2}{k_3c_0^2} \left(\frac{e^{i\Delta kL} - 1}{i\Delta k} \right), \quad (2.38)$$

where L describes the effective path length through the nonlinear system. The intensity is then obtained by calculating the time-averaged Poynting vector, which in our case yields

$$I_i = 2n_i\epsilon_0c_0 |A_i|^2, \quad \text{where } i = 1, 2, 3. \quad (2.39)$$

By inserting Equation (2.38) into (2.39) we obtain

$$I_3 = \frac{8n_3\epsilon_0d_{\text{eff}}^2w_3^4 |A_1|^2 |A_2|^2}{k_3^3c_0^3} \left| \frac{e^{i\Delta kL} - 1}{\Delta k} \right|^2, \quad (2.40)$$

where the squared modulus on the right side of this equation can be rewritten as

$$\begin{aligned} \left| \frac{e^{i\Delta kL} - 1}{\Delta k} \right|^2 &= L^2 \left(\frac{e^{i\Delta kL} - 1}{\Delta kL} \right) \left(\frac{e^{i\Delta kL} - 1}{\Delta kL} \right) = 2L^2 \frac{(1 - \cos\Delta kL)}{(\Delta kL)^2} \\ &= L^2 \frac{\sin^2(\Delta kL/2)}{(\Delta kL/2)^2} = L^2 \text{sinc}^2(\Delta kL/2). \end{aligned} \quad (2.41)$$

Finally, the intensity I_3 can be expressed in relation to the intensity of the incident fields by using Equation (2.39) to give the sought-after result

$$I_3 = \frac{2d_{\text{eff}}^2w_3^2I_1I_2}{n_1n_2n_3\epsilon_0c_0^3} L^2 \text{sinc}^2\left(\frac{\Delta kL}{2}\right). \quad (2.42)$$

The intensity I_3 scales with the incident field intensities and therefore a stronger non-linear process is achieved with stronger input fields. This expression also anticipates a sharp decrease in the efficiency of SFG when the perfect phase-matching condition is not fulfilled.

In general, perfect phase matching is problematic to accomplish because, for most materials, the refractive index monotonically increases as a function of frequency. Typically,

a phase-matching condition is achieved by using one of two techniques: either quasi-phase-matching or birefringent phase matching [7, 26]. In this Thesis, we employ nonlinear metamaterials to demonstrate an alternative phase matching method that is not possible in conventional materials.

2.2.5 Phase Matching in Metamaterials

A plasmon is a quantum of oscillation of the valence electrons in a conducting media. When plasmon oscillations are localized they can exhibit resonant behavior and create localized surface plasmon resonances (LSPRs). The resulting LSPRs give rise to strong electromagnetic fields close to the metal nanoparticles [8]. The local-field enhancements are very favorable in terms for nonlinear processes, which scale with higher powers of the electromagnetic field. The LSPRs depend strongly on numerous variables, such as the nanoparticle dimensions, shape, orientation and surrounding material [27]. As will soon be seen, the LSPRs are not only important for creating local field enhancements, but they are also important in fulfilling the phase-matching condition in metamaterials.

Our collaborators designed a metamaterial to be backward phase-matched by controlling the phase accumulation of the fundamental and SH waves as shown in Figure 2.1. The total accumulated phase for each wave is the sum of the phase shift bestowed by the metasurface δ_i (where $i = \omega$ or 2ω) and the phase shift accumulated from propagation through space φ_i [28].

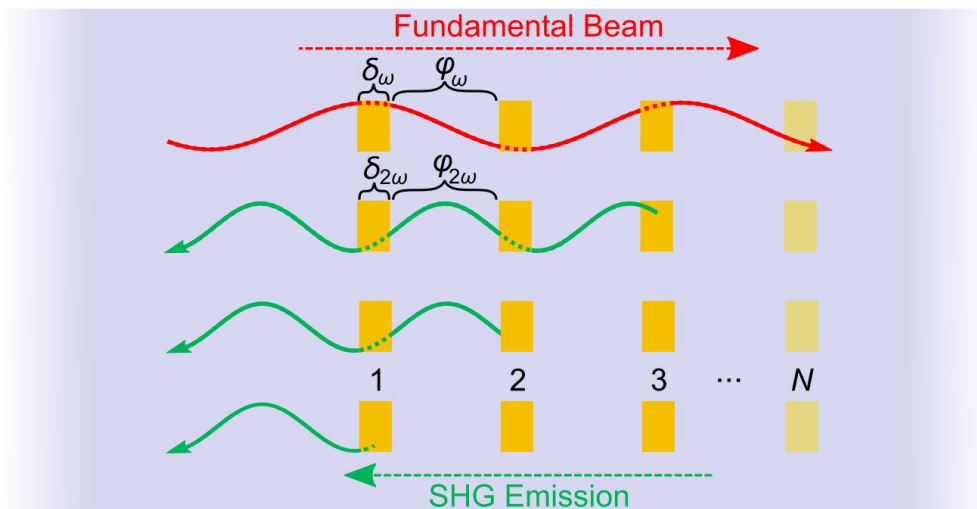


Figure 2.1. Backward phase-matched SHG emission from a metamaterial comprising of N stacked metasurfaces. When controlling the total phase accumulation of the fundamental beam (red arrow) and the SHG emissions (green arrows) the phase matching condition can be achieved. The total phase accumulation depends on the induced phase shifts caused by the metasurfaces (δ_ω and $\delta_{2\omega}$) and the phase accumulation due to propagation (φ_ω and $\varphi_{2\omega}$).

For our devices that are composed of metasurfaces separated by a distance of h , the

total phase accumulation should follow the relation

$$2(\varphi_\omega + \delta_\omega) + \varphi_{2\omega} + \delta_{2\omega} = 2\pi m, \quad (2.43)$$

where m is an integer and the accumulated propagation phases follow $\varphi_\omega = k_\omega h$ and $\varphi_{2\omega} = k_{2\omega} h$. From this equation it is now evident that δ_ω and $\delta_{2\omega}$ compensate for the wavevector mismatch. With careful designing of the metasurfaces, the phase-matching condition described by Equation (2.43) can be fulfilled by simply tuning the intersurface distance in the metamaterial.

The intensity of the SH field was shown to have a quadratic dependence on the effective path length through the nonlinear medium in Equation (2.42). Consequently, we would expect that the intensity of the SH field is directly related to the square of the number of layers in the phase-matched metamaterial.

3 RESEARCH METHODS

The purpose of the experiment was to investigate spectral nonlinear responses of two sets of metamaterial devices and demonstrate that such structures can be backward phase matched. In this chapter, we outline the samples studied, describe their fabrication methods, and present the experimental setup used to characterize their nonlinear optical properties.

3.1 Nanoparticle Array Samples

The metamaterial devices used in the experiments have one to five metasurfaces stacked on top of each other with a spacing of 225 nm as is shown in Figure 3.1. Each metasurface layer contains V-shaped gold nanoparticles with an arm width of 100 nm and an arm length of either 180 nm (L180-N) or 190 nm (L190-N). The V-shaped nanoparticles are noncentrosymmetric as required by SHG, and they were arranged into a square lattice with periodicity $p = 1000$ nm. Even though this lattice configuration has sparsely scattered particles across the metasurface, this configuration has been shown to greatly enhance SH emissions [15].

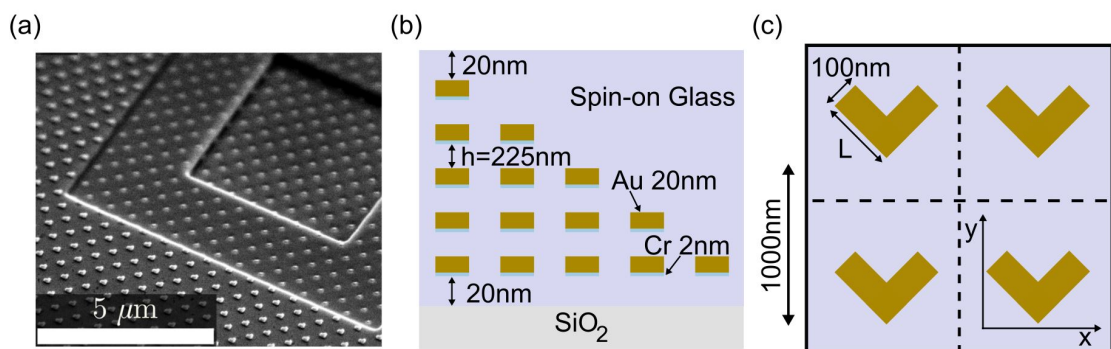


Figure 3.1. (a) Scanning electron micrograph showing the stacked nature of the metasurfaces from the samples that were studied. (b) Side view of the metamaterial with metasurface spacing $h = 225$ nm. (c) Each metasurface consisted of identical V-shaped gold nanoparticles with arm length L and 100 nm arm width. The nanoparticles were arranged into square lattice with $p = 1000$ nm.

The sample was fabricated at Pohang University of Science and Technology by Jeonghyun Kim, a student of Prof. Junsuk Rho. Despite the complex fabrication method shown in Figure 3.2, it allows for fabrication of nanostructures with precision approaching of a few nanometers. The sequence of fabrication steps can be iterated according to the number

of metasurface layers needed.

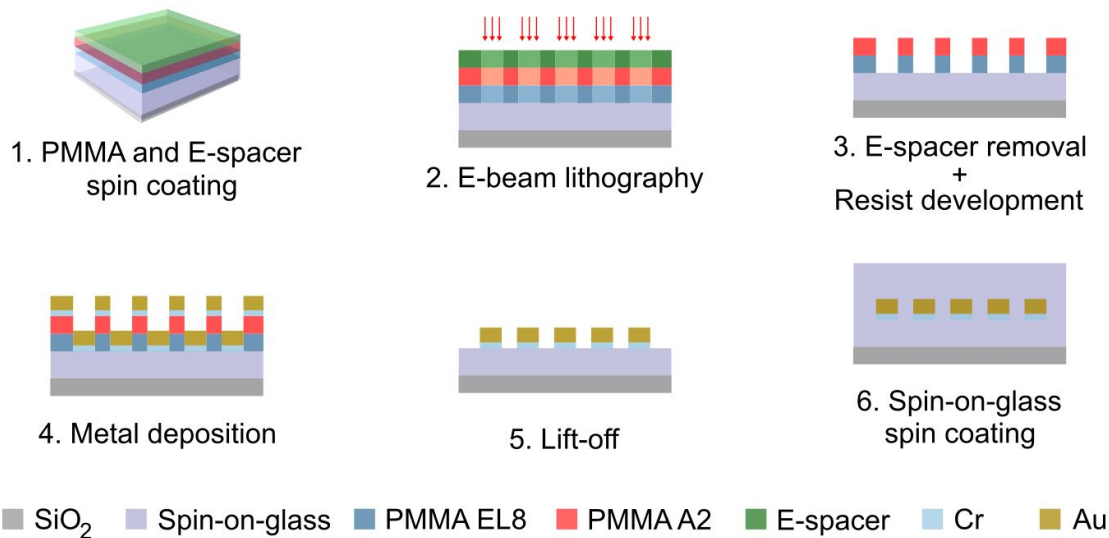


Figure 3.2. Schematic of nanolayer fabrication based on electron-beam lithography. The patterning process can be repeated according to the number of layers needed in the sample and it consists of the following six main steps. (1) spin coating of PMMA and E-spacer onto a clean substrate; (2) electron beam exposure; (3) E-spacer removal and resist development; (4) deposition of chromium and gold; (5) lift-off; (6) spin coating of spin-on-glass.

To begin the process, two uniform polymethyl methacrylate (PMMA) films are separately spin-coated and baked on top of a clean silicon dioxide substrate. First, PMMA EL8 is spin coated at 5000 rpm speed for one minute and then baked at 150 °C for five minutes. The same steps are made for PMMA A2, but it is spin-coated at 2000 rpm and baked at 180 °C. Because of the negative charge that can build up on the surface of the sample when performing electron-beam lithography, a conductive polymer called E-spacer is also spin-coated onto the surface of the sample at 2000 rpm for one minute. Next, the outline of the particles is drawn into the positive resist stack by performing electron-beam lithography. The E-spacer is immediately removed by placing the sample into a distilled water bath for one minute. Now, the resist can be developed in a 3:1 mixture of isopropanol and methyl isobutyl ketone at 0 °C for 12 minutes and then rinsed with isopropanol. After the resist has been patterned, thin layers of gold (20 nm) and adhesive chromium (3 nm) are deposited through e-beam evaporation at 1 Å/s. Lift-off is carried out with an acetone bath at 50 °C for one minute. Finally, a layer of coating dielectric IC1-200 is spin coated at 6000 rpm for one minute and then baked at 250 °C for 5 minutes, to obtain a spacer layer between the nanoparticle metasurfaces.

The particles were made out of gold because it is an inert metal with well-known plasmonic properties. As already explained in Section 2.2.5, the plasmon resonances dictate the changes in phase behavior. With the chosen nanoparticle dimensions and lattice configuration, these samples were designed to exhibit LSPRs between 1000–1100 nm. Under these conditions, the perfect phase-matching condition is satisfied close to the LSPR frequency when the space between the metasurfaces is $h = 225$ nm. For sample

L180-*N* the phase-matching condition was set to be fulfilled for input linear polarization orthogonal to the symmetry axis of the V-particles (*x*-axis), while for sample L190-*N* the same should happen, but for input linear polarization along the symmetry axis (*y*-axis).

3.2 Experimental Setup and Procedure

With the setup shown in Figure 3.3, a laser beam was focused on a sample and SH emission spectra were measured. An optical parametric oscillator (OPO) pumped with a titanium-sapphire laser was used to produce the fundamental beam incident on the sample. The pulsed mode-locked laser used as the excitation source was a Chameleon Vision II by Coherent and it was set to operate at a 780 nm wavelength with a pulse duration of 220 fs and a repetition rate of 82 MHz. The Chameleon Compact OPO by Coherent provided wide wavelength tunability and made it possible to access the wavelengths in the desired near-infrared range (1000–1300nm).

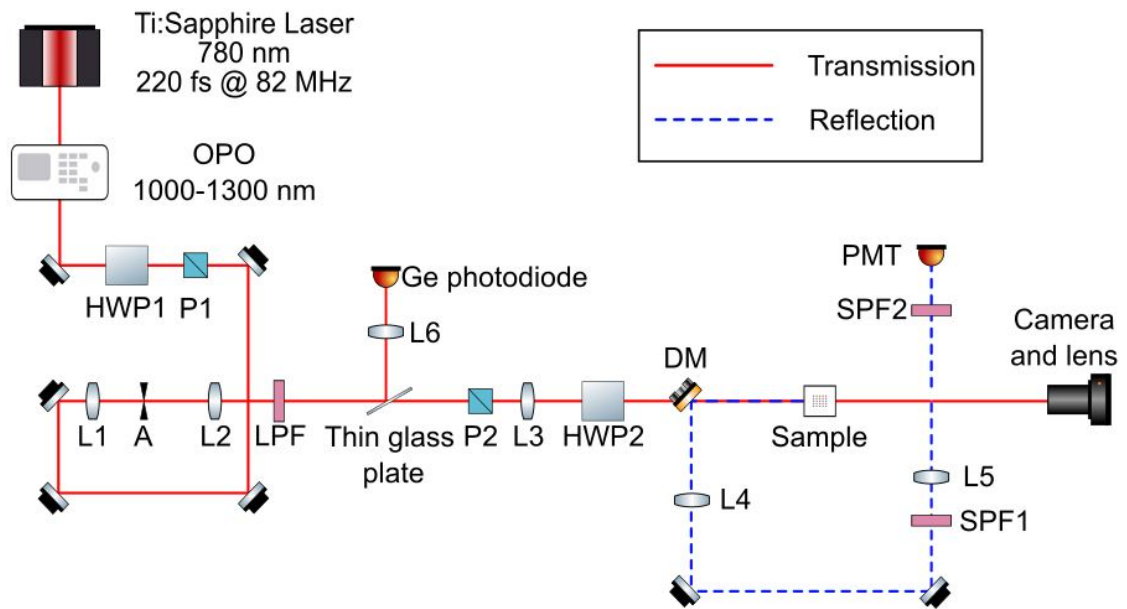


Figure 3.3. The experimental setup for measuring backward SHG emissions from a sample. The setup contains lenses (L1–L6), half-wave plates (HWP1–HWP2), an aperture (A), polarizers (P1–P2), a long-pass filter (LPF), short-pass filters (SPF1–SPF2), dichroic mirror (DM) and photomultiplier tube (PMT). The solid red line shows the path for the fundamental beam and the dashed blue line shows the path for the generated back-propagating SH beam.

Throughout the setup, light passes through multiple lenses to focus and spread out light. The lenses, as well as other optical components in the main beam path, are numbered in ascending order according to their distance from the laser. All of the lenses are made by Thorlabs, and they are achromatic, which means they are specially designed to have equal focal lengths for different wavelengths. The combination of the first (AC127-030-C-ML) and second lens (AC254-150-C-ML) expand the incident light to five times its original size, while the pinhole (A) between them acts as a spatial filter to clean up aberrations in the optical system. The beam expansion is essential because it provides a larger field-of-

view when imaging the sample and helps create a smaller laser focal spot diameter at the sample plane where the third lens (AC254-150-C-ML) focuses. Lens L4 (AC254-100-A-ML) collects the SHG emissions from the sample, while lens L5 (AC254-200-A) focuses the light into the photon counting apparatus.

Optical filters selectively block light at specific ranges of wavelengths. A long-pass filter LPF (FEL0900) was placed before the sample, in order to selectively block out any non-linear signals produced by optical components that are placed before the sample. Two short-pass filters SPF1 (FGS900-A) and SPF2 (FESH0900) are used after the sample to ensure that undesirable background light is not measured. The dichroic mirror also acts as a filter. It not only allows for the fundamental beam to pass through the sample to the camera, but it also reflects the backward SHG emissions towards the photon detector.

The detector used in the setup was a photomultiplier tube (PMA-C 192-M) by PicoQuant that contains a preamplifier, thermoelectric cooler, and an internal shutter. The PMT typically creates a current pulse whenever a single photon is detected. However, sometimes small electric currents can flow through the PMT even when no photons are entering the device. In order to decrease the rate of dark counts caused by dark currents, the PMT has to be cooled for about five minutes with the thermoelectric cooler before any measurements are taken. After the PMT has reached a stable temperature, the dark counts can still be varied anywhere between 570 and 750 counts per second. For this reason, the SHG readings have to be fixed by subtracting the average dark counts from them.

To begin the experiments, a complementary metal-oxide semiconductor camera was used to align the sample and fundamental beam appropriately. Due to the camera lacking sensitivity at longer wavelengths, the alignment of the sample had to be done by setting the fundamental wavelength to 1060 nm. This ensured that the camera was able to create an image of the sample. Afterwards, the camera was manually focused on the same plane where L3 focused the fundamental beam. This was achieved by making the laser beam image as small as possible while having the beam still maintain its circular profile. The laser beam area was then drawn on the camera software so that the sample could be moved with a translation stage directly into the correct focal point.

After placing the sample into its correct position, the input power and polarization needed to be set for the measurements. The fundamental beam power incident at the sample plane was monitored indirectly by a germanium photodiode. In order to avoid permanently damaging the sample, the input power of the laser was set to 10 mW. This was controlled continuously with a linear polarizer (P1) and a half-wave plate (HWP1) set up on a computer-controlled motorized rotation stage. The second polarizer (P2) located closer to the sample helped to correct polarization deformations that may have occurred from the optical path between P1 and P2. The final input polarization for the sample was controlled by the second half-wave plate (HWP2) and it was selected according to which metamaterial device, L180-N or L190-N, was being measured (see Section 3.1).

We subsequently measured the SHG emission spectra from different metamaterial de-

vices consisting of varying number of metasurfaces by performing multiple wavelength scans. A typical wavelength scan would consist of iteratively changing the wavelength of the OPO, adjusting the input power until it is stable, and then recording the PMT photon counts. Because the metamaterial devices contained 1–5 metasurfaces stacked on top of each other, five sets of data were measured per device.

4 RESULTS AND DISCUSSION

The metamaterial devices were classified into two categories based on their nanoparticle arm length, L180- N and L190- N . The SHG emission power spectra for the different number of layers is shown for both samples in Figure 4.1. Straightaway it can be observed that the two samples have very comparable features. The overall trend indicates an increase in the average SHG power when the number of layers grow. With the 10 mW input fundamental beam power, SHG emission power was produced in the order of femtowatts, with the strongest SHG signal coming from L180-5 with a power of 71 fW.

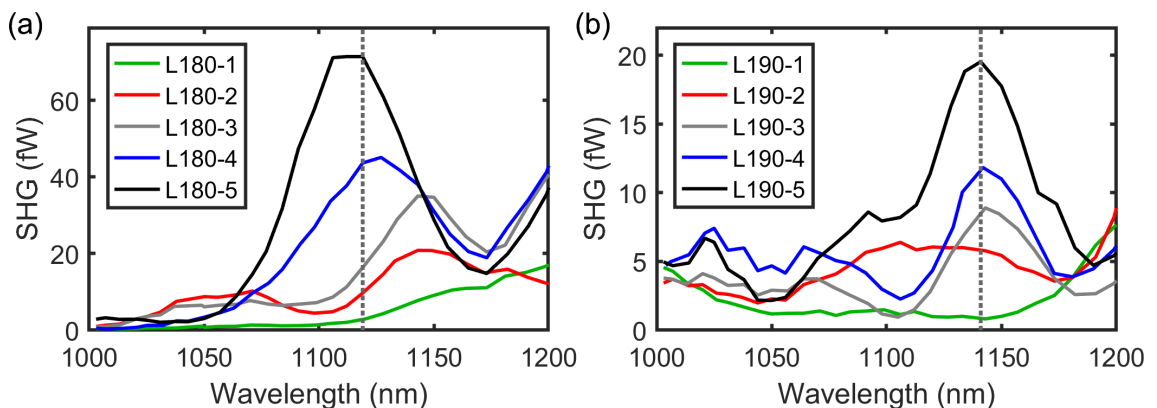


Figure 4.1. The reflected SHG emission power was detected as a function of the fundamental wavelength for two different samples (a) L180- N and (b) L190- N . The vertical dashed line represents the pump wavelength at which strong constructive phase matching occurs for the different samples.

The SHG peaks increasing in strength as a function of stack amount suggest phase matching is occurring between 1100–1150 nm. Destructive phase matching can be seen occurring between 1000–1050 nm, because at these wavelengths the SH signals do not grow as a function of N . Upon closer inspection, the strongest constructive phase matching happens at 1119 nm for L180- N and 1141 nm L190- N . These wavelengths are marked in Figure 4.1 with vertical dashed lines and they can be used in order to calculate the enhancement of SHG during constructive phase matching.

In Figure 4.2, the blue squares and red circles represent the enhancements that were normalized to each of the samples' own monolayer SHG power, L180-1 and L190-1, respectively. From here it can already be deduced that a multilayer arrangement increases the second-harmonic response as compared to a single metasurface. By fitting different functions through the plot, we see that the enhancement does not depend linearly on the

number of layers as shown by the gray dashed line, but it instead follows the quadratic dependence shown with the solid gray line.

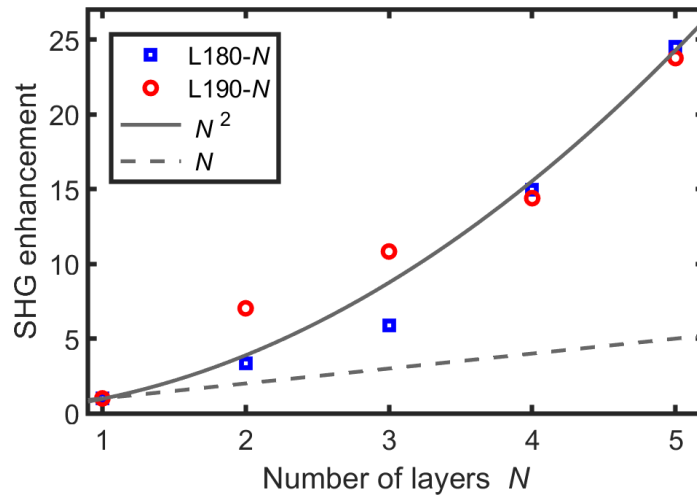


Figure 4.2. Calculated SHG intensity enhancement as a function of the number of layers at 1119 nm for L180-N (blue squares) and 1141nm for L190-N (red circles). The enhancement for both samples is normalized to the SHG intensity from each of the samples own monolayer measurement ($N = 1$). The enhancement does not depend linearly on N (gray solid line), but rather follows the expected quadratic dependence on N (gray dotted line).

In addition to the quadratic dependence, it is also evident that the SHG peaks in Figure 4.1 (a) are blueshifted over 30 nm. This could be due to the optical coupling of adjacent metasurfaces [29]. The same effect is most likely responsible for the exceptional 25-fold enhancement in SHG. According to the well known Kramers–Kronig relations, all resonating structures are inclined to exhibit losses [30]. The fact that no apparent losses were observed under these circumstances indicates a radiative coupling phenomena may have occurred between neighbouring metasurfaces [31, 32]. Another possibility is, that there were minor differences in the SHG emission among the metasurfaces located in different samples. To elaborate further, the 25-fold originates from the normalization to the monolayer samples, but because each measurement was performed with a different sample, there is a chance that the first metasurface in each of the samples did not behave exactly in the same way. The same logic also applies to the other metasurfaces located in different samples as well.

5 CONCLUSION

In this work, enhancements of second-order nonlinear optical processes in three-dimensional metamaterials were studied. With the help of theoretical knowledge and straightforward measurements, we experimentally demonstrated a unique phase-matching technique for back-propagating SHG in three-dimensional metamaterials. The technique was based on controlling the total accumulated phase for the fundamental and second-harmonic waves using phase-engineering techniques.

A general agreement between the measured SHG emission power spectra and the calculated SHG enhancement validate that our samples were appropriately fabricated to fulfill the phase-matching condition. In the end, the results showed roughly a 25-fold enhancement of second-harmonic emissions from a metamaterial fabricated by stacking five metasurfaces on top of each other as compared to a metamaterial with a single metasurface. Another important result worth mentioning was the challenging backward direction of the SH emissions. Using conventional nonlinear crystals such configuration is not possible and would require more complicated quasi-phase-matching techniques.

There are two main physical points that contribute to the realization of the observed effects. First and foremost, the geometry of the nanoparticles and separation between the nanolayers allowed for the phase-matching condition to be achieved. Secondly, the ability of the metasurfaces to achieve radiative coupling with each other resulted in further enhanced nonlinear response.

In the future, it would be compelling to reproduce the results with a sample that has more metasurfaces. This type of research is important for the development of nanophotonics and it could be essential for designing metamaterials where the plasmonic field enhancements and phase matching compensate the reduced nonlinear interaction lengths. Unfortunately with the nanofabrication techniques of today, even producing a three-dimensional sample with just five layers is tedious work. Therefore, alternative nanostructures and techniques should be looked into for SHG enhancement. Keeping this in mind, a realistic topic for future work could be achieving higher conversion efficiencies by placing our sample into a multi-pass cavity.

To conclude, metamaterials can be tedious to design and manufacture, but they are also expected to have prodigious advantages at the nanoscale. With new information about nonlinear responses and advanced optical functionalities, we can improve the performance and design of photonic nanostructures. To this day, nonlinear optics has gained

countless applications and hopefully, by expanding on the limits of nanoscale nonlinear plasmonics, we will be able to fully exploit the potential of plasmonic metamaterials for useful technological innovations.

REFERENCES

- [1] Y. Shen. *The Principles of Nonlinear Optics*. Pure & Applied Optics Series: 1-349. Wiley, 1984.
- [2] E. Garmire, "Nonlinear optics in daily life," *Opt. Express*, **21**, 30532–30544 (2013).
- [3] G. Bautista, M. J. Huttunen, J. Mäkitalo, J. M. Kontio, J. Simonen and M. Kauranen, "Second-harmonic generation imaging of metal nano-objects with cylindrical vector beams," *Nano Lett.*, **12**, 3207–3212 (2012).
- [4] C. Li. *Nonlinear Optics: Principles and Applications*. Springer Singapore, 2016.
- [5] P. A. Franken, A. E. Hill, C. W. Peters and G. Weinreich, "Generation of Optical Harmonics," *Phys. Rev. Lett.*, **7**, 118–119 (4 1961).
- [6] T. H. Maiman, "Stimulated optical radiation in ruby," *nature*, **187**, 493–494 (1960).
- [7] N. M. Litchinitser, "Nonlinear optics in metamaterials," *Advances in Physics: X*, **3**, 1367628 (2018).
- [8] S. A. Maier. *Plasmonics: fundamentals and applications*. Springer Science & Business Media, 2007.
- [9] M. Kauranen and A. V. Zayats, "Nonlinear plasmonics," *Nat. Photonics*, **6**, 737–748 (2012).
- [10] J. Lee, M. Tymchenko, C. Argyropoulos, P. Y. Chen, F. Lu, F. Demmerle, G. Boehm, M. C. Amann, A. Alù and M. A. Belkin, "Giant nonlinear response from plasmonic metasurfaces coupled to intersubband transitions," *Nature*, **511**, 65–69 (2014).
- [11] A. Krasnok, M. Tymchenko and A. Alù, "Nonlinear metasurfaces: a paradigm shift in nonlinear optics," *Mater. Today*, **21**, 8–21 (2018).
- [12] M. W. Klein, C. Enkrich, M. Wegener and S. Linden, "Second-harmonic generation from magnetic metamaterials," *Science (80-.)*, **313**, 502–504 (2006).
- [13] A. Alù, M. G. Silveirinha, A. Salandrino and N. Engheta, "Epsilon-near-zero metamaterials and electromagnetic sources : Tailoring the radiation phase pattern," *Phys. Rev. B*, **75**, 155410 (2007).
- [14] S. Zhang, Y.-S. Park, J. Li, X. Lu, W. Zhan and X. Zhang, "Negative index in chiral metamaterials," *Phys. Rev. Lett.*, **102**, 023901 (2009).
- [15] R. Czaplicki, A. Kiviniemi, M. J. Huttunen, X. Zang, T. Stolt, I. Vartiainen, J. Butet, M. Kuittinen, O. J. F. Martin and M. Kauranen, "Less is more enhancement of second-harmonic generation from metasurfaces by reduced nanoparticle density," *Nano Lett.*, **18**, 7709–7714 (2018).
- [16] M. J. Huttunen, R. Czaplicki and M. Kauranen, "Nonlinear plasmonic metasurfaces," *J. Nonlinear Opt. Phys. Mater.*, **28**, 1950001 (2019).
- [17] M. Kauranen, "Physics. Freeing nonlinear optics from phase matching," *Science (New York, N.Y.)*, **342**, 1182–1183 (2013).

- [18] G. Li, S. Chen, N. Pholchai, B. Reineke, P. W. H. Wong, E. Y. B. Pun, K. W. Cheah, T. Zentgraf and S. Zhang, "Continuous control of the nonlinearity phase for harmonic generations," *Nat. Mater.*, **14**, 607–612 (2015).
- [19] G. Li, S. Zhang and T. Zentgraf, "Nonlinear photonic metasurfaces," *Nat. Rev. Mater.*, **2**, 1–14 (2017).
- [20] R. Sutherland. *Handbook of Nonlinear Optics*. Optical Science and Engineering. Taylor & Francis, 2003.
- [21] E. Hecht. *Optics, Fourth Edition*. Pearson education. Addison-Wesley, 2002.
- [22] R. W. Boyd. *Nonlinear Optics, Third Edition*. 3rd. USA: Academic Press, Inc., 2008.
- [23] S. Solgi, M. Tafreshi and M. Ghamsari, "Nonlinear Optical Crystals for Second Harmonic Generation," *Crystallography Reports*, **64**, 1138–1149 (2019).
- [24] B. K. Canfield, S. Kujala, K. Jefimovs, J. Turunen and M. Kauranen, "Linear and nonlinear optical responses influenced by broken symmetry in an array of gold nanoparticles," *Opt. Express*, **12**, 5418 (2004).
- [25] H. Husu, J. Mäkitalo, J. Laukkanen, M. Kuittinen and M. Kauranen, "Particle plasmon resonances in L-shaped gold nanoparticles," *Opt. Express*, **18**, 16601–16606 (2010).
- [26] M. Fejer, G. Magel, D. Jundt and R. Byer, "Quasi-phase-matched second harmonic generation: tuning and tolerances," *IEEE Journal of Quantum Electronics*, **28**, 2631–2654 (1992).
- [27] R. Czaplicki, J. Mäkitalo, R. Siikanen, H. Husu, J. Lehtolahti, M. Kuittinen and M. Kauranen, "Second-harmonic generation from metal nanoparticles: Resonance enhancement versus particle geometry," *Nano Lett.*, **15**, 530–534 (2015).
- [28] P. Genevet, F. Capasso, F. Aieta, M. Khorasaninejad and R. Devlin, "Recent advances in planar optics: from plasmonic to dielectric metasurfaces," *Optica*, **4**, 139 (2017).
- [29] M. J. Huttunen, K. Dolgaleva, P. Törmä and R. W. Boyd, "Ultra-strong polarization dependence of surface lattice resonances with out-of-plane plasmon oscillations," *Opt. Express*, **24**, 28279–28289 (2016).
- [30] A. McGurn. *Nonlinear Optics of Photonic Crystals and Meta-materials*. Morgan & Claypool Publishers, 2015.
- [31] M. J. Huttunen, P. Rasekh, R. W. Boyd and K. Dolgaleva, "Using surface lattice resonances to engineer nonlinear optical processes in metal nanoparticle arrays," *Phys. Rev. A*, **97**, 053817 (2018).
- [32] M. J. Huttunen, O. Reshef, T. Stolt, K. Dolgaleva, R. W. Boyd and M. Kauranen, "Efficient nonlinear metasurfaces by using multiresonant high-Q plasmonic arrays," *J. Opt. Soc. Am. B*, **36**, E30–E35 (2019).